scientific reports

Check for updates

OPEN

Elucidating the molecular basis of Brunner syndrome: how clinically relevant mutations disrupt serotonin binding and active-site stability in monoamine oxidase A

Martina Rajić[1,2], Jernej Stare[2], Lucija Vrban Đerek[3], Marija Sollner Dolenc[1], Janez Mavri[2] & Robert Vianello[3]✉

Monoamine oxidase A (MAO-A) is a key enzyme responsible for serotonin degradation and mutations in the *MAOA* gene are associated with impaired enzymatic function and neuropsychiatric disorders, including Brunner syndrome. Although previous studies have demonstrated that such mutations reduce catalytic efficiency, their effects on substrate binding remain poorly understood. Here, we employed an integrated computational approach combining molecular docking, molecular dynamics simulations, and MM-GBSA binding free energy calculations to investigate the impact of four clinically relevant MAO-A variants (C266F, V244I, E446K, and R45W) on serotonin binding and active-site stability. Using a one-substrate, multiple-variant framework, we systematically compared disease-associated MAO-A variants and identified both shared and mutation-specific mechanisms affecting ligand recognition. All investigated mutants exhibited reduced serotonin binding affinity relative to the wild-type enzyme, as reflected by positive ΔΔ*G* values. Structural and energetic analyses revealed that this loss of affinity does not arise from major conformational changes but from mutation-induced perturbations of protein dynamics. Increased flexibility of second-shell residues promoted enhanced breathing of the binding pocket, leading to greater solvent-accessible surface area and increased water penetration into the active site. Consequently, the hydrophobic environment required for efficient substrate stabilization was compromised, weakening key hydrogen-bonding and electrostatic interactions. Residue-level energy decomposition identified unfavorable electrostatic contributions involving the FAD cofactor and active-site residues such as Tyr444 and Gln215 as major determinants of reduced binding affinity. Overall, our results demonstrate that mutation-induced changes in protein dynamics, hydration, and electrostatics collectively impair serotonin binding in MAO-A, providing molecular-level insight into the functional consequences of Brunner syndrome-associated mutations.

Keywords Monoamine oxidase A, Brunner syndrome, Ligand binding, Molecular dynamics, Active-site hydration, Electrostatics

Monoamine oxidases (MAO's) are flavoenzymes that play a central role in the degradation of numerous amines, including key monoamine neurotransmitters such as dopamine, serotonin, and noradrenaline[1]. The enzyme occurs in two isoforms, MAO–A and MAO–B, each characterized by distinct substrate preferences, inhibitor sensitivities, and cellular and tissue distribution[2]. Although MAO enzymes are mainly localized in neurons and astroglial cells of the central nervous system, they are also widely distributed in peripheral tissues[3]. MAO–A is mainly associated with the gastrointestinal tract, lung, liver, and placenta, while MAO–B is predominantly found in platelets and accounts for the majority of MAO enzyme activity in the brain[4,5]. The cavity in the MAO–B enzyme is divided into two regions, the substrate and entrance cavities, which can switch between "open" and "closed"

[1]Faculty of Pharmacy, University of Ljubljana, Aškerčeva Cesta 7, 1000 Ljubljana, Slovenia. [2]Theory Department, Laboratory for Computational Biochemistry and Drug Design, National Institute of Chemistry, Hajdrihova Ulica 19, 1000 Ljubljana, Slovenia. [3]Laboratory for the Computational Design and Synthesis of Functional Materials, Division of Organic Chemistry and Biochemistry, Ruđer Bošković Institute, Bijenička Cesta 54, 10000 Zagreb, Croatia. ✉email: Robert.Vianello@irb.hr

states depending on the positioning of Ile199[6,7]. Among substrates of MAO, serotonin (5-hydroxytryptamine, 5-HT) is preferentially oxidized by MAO-A, whereas phenylethylamine and benzylamine are preferentially oxidized by MAO-B. In general, most of MAO substrates (e. g., dopamine, tyramine, tryptamine as well as the aforementioned serotonin, phenylethylamine and benzylamine) can be metabolized by both MAO-A and MAO-B, but not necessarily with the same efficiency by the two isoforms. Their apparent isoform selectivity depends on substrate concentration, tissue-specific MAO-A/MAO-B abundance, and the kinetic parameters of each isoform[8]. On the other hand, detailed crystallographic analyses have revealed that the active site of MAO–A consists of a single, compact, and predominantly hydrophobic cavity extending from the flavin adenine dinucleotide (FAD) cofactor toward the protein surface, with an estimated volume of approximately 550 Å3 in the clorgyline–bound structure[9,10]. The flavin adenine dinucleotide (FAD) cofactor is covalently attached via an 8α–S–cysteinyl linkage to Cys406, and its isoalloxazine ring adopts a bent conformation about the N(5)–N(10) axis, introducing strain that may have catalytic relevance. In addition, the amide linkage between Cys406 and Tyr407 is found in a cis conformation, while the flavin side chains adopt extended conformations characteristic of flavoenzymes[7,10,11]. Within the active site, Tyr407 and Tyr444 form a conserved aromatic pair positioned on the *re face* of the flavin isoalloxazine ring, stabilizing the substrate and contributing to its proper orientation for reaction, while Lys305 is hydrogen–bonded to the N(5) atom of the flavin via a bridging water molecule, forming part of a conserved interaction network[7,10]. Structural comparisons between MAO–A and MAO–B have identified key determinants of substrate and inhibitor selectivity, particularly the Phe208–Ile335 pair in MAO–A compared to the Ile199–Tyr326 pair in MAO–B. Unlike Ile199 in MAO–B, which acts as a gating residue controlling cavity opening, Phe208 in MAO–A does not exhibit such behavior, resulting in a single, monopartite active site cavity[6]. High–resolution structural and mutagenesis studies have demonstrated that access to the active site is regulated by a narrow entrance channel formed by multiple loop regions (Val93–Glu95, Tyr109–Pro112, and Phe208–Asn212), with residues spanning 108–118, particularly Gly110, playing a critical role in maintaining the conformational flexibility required for efficient substrate binding[10]. Based on the three–dimensional structure of human monoamine oxidase A, the active site is defined by a set of residues lining the substrate–binding cavity, including Tyr69, Gln74, Val91, Val93, Leu97, Ile180, Asn181, Ile207, Phe208, Ser209, Val210, Glu216, Cys323, Ile325, Ile335, Leu337, Met350, Phe352, Tyr407, and Tyr444, which collectively determine the physicochemical properties of the binding environment[9]. Further insights from the MAO–A–harmine complex revealed that the inhibitor is stabilized by an extended interaction network involving residues such as Tyr69, Asn181, Phe208, Val210, Gln215, Cys323, Ile325, Ile335, Leu337, Phe352, Tyr407, Tyr444, and the FAD cofactor, highlighting the importance of both hydrophobic and π–π interactions in ligand binding, with Ile335 playing a key role in modulating substrate and inhibitor selectivity[10]. Site–directed mutagenesis studies have identified several key residues essential for MAO–A catalytic activity, including Lys305, Trp397, Tyr407, and Tyr444, whose substitution leads to a significant reduction in enzymatic function. These residues play a crucial role in maintaining the structural and electronic environment required for reaction[12]. Together, these findings highlight that the MAO–A active site represents a finely tuned environment in which even subtle perturbations, such as those introduced by mutations, can significantly impact substrate binding and catalytic efficiency.

At the genetic level, the genes encoding the two MAO isoenzymes (MAO–A and MAO–B) are located on the X chromosome[13]. Consequently, mutations in the MAO–A gene can significantly impair enzyme activity and are associated with Brunner syndrome, (OMIM #300615), a rare X–linked disorder first described by H. G. Brunner et al. in 1993 in a large Dutch family, characterized by reduced degradation of monoamine neurotransmitters[4,13]. Analysis of the affected individuals revealed that the observed behavioral abnormalities were linked to MAO–A deficiency, and genetic sequencing identified a mutation in the *MAOA* gene present in all affected males. This mutation, c.886C > T (p.Q296*), introduces a premature stop codon, leading to the production of a truncated and nonfunctional enzyme. As a consequence, these loss–of–function mutations disrupt monoamine metabolism, resulting in elevated levels of serotonin, dopamine, and noradrenaline, which have been associated with behavioral abnormalities such as impulsivity, aggression, and mild intellectual disability[4,13,14]. Further studies have led to the identification of additional *MAOA* variants associated with neurodevelopmental disorders. One of the first reported was the c.797_798delinsTT (p.C266F) missense mutation, described by Piton et al.[15], which was detected in a boy diagnosed with autism spectrum disorder, attention deficit, and autoaggressive behavior. Notably, two of his maternal uncles carrying the same mutation showed severe intellectual disability and a history of early–life maltreatment. Biochemical analyses revealed significant alterations in monoamine metabolism, including elevated urinary normetanephrine (NMN) and metanephrine (MN), along with reduced levels of vanillylmandelic acid (VMA), as well as markedly decreased plasma concentrations of 5–hydroxyindoleacetic acid (5–HIAA) and 3,4–dihydroxyphenylglycol (DHPG). Another variant, c.133C > T (p.R45W), was reported by Palmer et al.[16] in a family in which affected males exhibited borderline to mild intellectual disability, attention deficits, and impaired social functioning. In one individual, this phenotype was accompanied by episodes of explosive aggression, as well as intermittent physiological symptoms such as flushing, headaches, and diarrhea. Biochemical analyses revealed elevated serotonin and normetanephrine levels, together with reduced levels of degradation products such as 5–hydroxyindoleacetic acid (5–HIAA) and vanillylmandelic acid (VMA). More recently, Popp et al.[17], identified the c.730G > A (p.V244I) variant using high–throughput sequencing in a 7–year–old boy presenting with speech delay, moderate intellectual disability, and behavioral disturbances. Similarly, the c.1336G > A (p.E446K), reported by Peters et al.[18], was identified in a 7–year–old boy presenting with borderline intellectual disability and behavioral abnormalities, including aggressive and antisocial behavior. Biochemical analyses revealed elevated levels of serotonin, dopamine, and norepinephrine in serum and urine, consistent with markedly reduced MAO–A activity. Reduced MAO–A activity has been associated with elevated serotonin levels, potentially arising even during prenatal development, which may lead to persistent changes in neuroplasticity that are difficult to reverse pharmacologically. These observations suggest that impaired catalytic

function of MAO–A plays a central role in disrupting neurotransmitter homeostasis and contributes to the development of neurodevelopmental disorders.

To provide a concise clinical and molecular overview, the previously reported phenotypes, biochemical findings, inheritance patterns, functional evidence, and pathogenicity classifications of the investigated MAOA variants are summarized in Table 1. All investigated MAOA variants are classified as pathogenic or likely pathogenic, in agreement with the reported clinical phenotypes and, where available, the corresponding biochemical and functional evidence. These data support the clinical relevance of the selected variants and their association with impaired MAO-A function, altered monoamine metabolism, and neurodevelopmental and behavioral abnormalities.

Previous computational studies employing empirical valence bond (EVB) simulations, have demonstrated that mutations in MAO–A can lead to reduced catalytic efficiency, resulting in slower reaction rates[19–21]. Building on this mechanistic foundation, the present work addresses the complementary question of how such mutations influence substrate binding. Because catalytic turnover depends not only on the chemical step but also on effective substrate recognition and positioning, integrating both aspects is essential for a comprehensive description of enzyme function. Here, molecular dynamics simulations combined with binding affinity calculations are used to characterize the impact of mutations on enzyme–substrate interactions, active-site architecture, and overall structural stability. To address this issue, we employed a computational strategy focused on the natural MAO–A substrate, serotonin, to investigate how clinically relevant point mutations of MAO–A influence enzyme–substrate interactions. Initially, molecular docking simulations were performed to obtain plausible binding poses of serotonin within the active site of both wild–type and mutant MAO–A variants. The resulting complexes were then subjected to classical molecular dynamics (MD) simulations to explore their structural stability and dynamic behavior over time. Binding affinities were estimated using the Molecular Mechanics/Generalized Born Surface Area (MM–GBSA) approach, allowing for a quantitative comparison between the wild–type enzyme and its variants. In addition, per–residue energy decomposition analysis was carried out to identify key amino acid residues contributing to substrate binding. Complementary analyses, including hydrogen bond networks, solvent–accessible surface area (SASA), and water molecule occupancy, were performed to evaluate the impact of mutations on the local environment of the active site. This integrated approach provides detailed insight into how specific mutations modulate substrate affinity and complements previous findings related to their impact on catalytic activity.

Results and discussion

Evolutionary conservation of the mutation sites

Prior to the structural analysis, the evolutionary conservation of the mutated residues was evaluated by multiple sequence alignment (MSA) of representative vertebrate MAO-A orthologs from 15 representative vertebrate species including human, non-human primates, domestic and laboratory mammals, birds, an amphibian, and fish as shown in Fig. 1. Arg45, Val244, and Glu446 were completely conserved across all analyzed sequences, indicating that these positions are under strong evolutionary constraint and are therefore likely important for maintaining MAO-A structure and function. Cys266 was conserved among mammalian orthologs, whereas alanine or glycine occurred at the corresponding position in non-mammalian vertebrates. This pattern suggests that, although cysteine itself is not universally required in all analyzed species, position 266 preferentially accommodates a small amino-acid side chain and is likely structurally constrained. Consequently, substitutions at these conserved or size-restricted positions may perturb local interactions, protein packing, cofactor binding, or conformational stability. In particular, the C266F substitution introduces a markedly bulkier aromatic

MAOA variant	MAO-A mutation	Reported phenotype	Biochemical findings	Inheritance/segregation	Classification*	References
c.797_798delinsTT	*p.C266F*	Autism spectrum disorder Attention problems Self-injurious behavior Severe ID in maternal uncles	Impaired catecholamine and serotonin metabolism; markedly reduced MAO-A activity and an approximately three-fold decrease in MAO-A protein levels in patient fibroblasts	The variant was inherited from a heterozygous mother and was present in the proband and two affected maternal uncles	Pathogenic	Piton et al.[15] PMID: 24169519
c.133C>T	*p.R45W*	Borderline to mild ID Attention deficits Impaired social functioning Impulsive or violent behaviour	Biochemical profile consistent with MAO-A deficiency, including elevated serotonin, metanephrine, and normetanephrine and reduced vanillylmandelic acid	Present in two affected males and their symptomatic heterozygous mother; absent from the maternal grandmother	Pathogenic/ likely pathogenic	Palmer et al.[16] 25807999
c.730G>A	*p.V244I*	Speech delay Moderate ID Behavioral problems	No supporting biochemical or functional evidence of MAO-A deficiency was reported; the variant was identified by exome sequencing and confirmed by Sanger sequencing	Maternally inherited in an affected male; skewed X-chromosome inactivation was reported in the mother	Likely pathogenic	Popp et al.[17], PMID: 29158550
c.1336G>A	*p.E446K*	Mild ID (IQ 69) Temper tantrums Yelling Aggressive and antisocial behavior including violence and property damage	Biochemical hallmarks of MAO-A deficiency, with increased monoamines and metabolites in serum and urine; MAO-A activity was almost completely absent in patient fibroblasts	Reported as de novo in a male patient with a negative family history	Likely pathogenic	Peters et al.[18], PMID: 33728254

Table 1. Previously clinical and molecular evidence reported for the investigated MAOA variants. Classification was obtained from ClinVar where a dedicated variant record was available or from the original clinical publication when no dedicated ClinVar classification was identified.

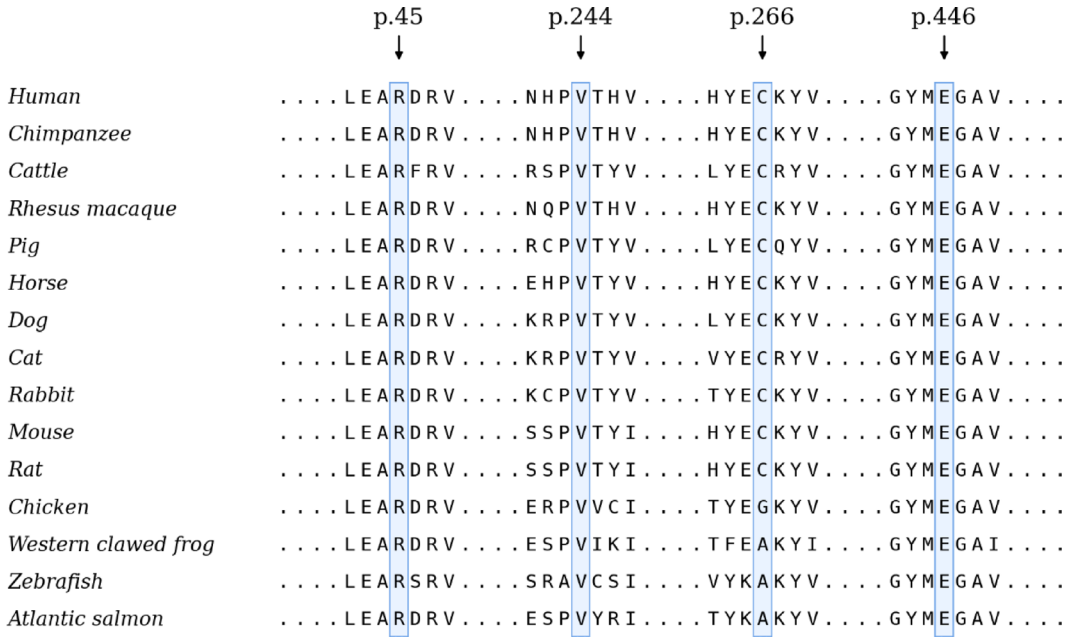


Fig. 1. Multiple sequence alignment and conservation of investigated MAO-A residues. Only the relevant sequence regions surrounding Arg45, Val244, Cys266, and Glu446 are shown for MAO-A orthologs from 15 representative vertebrate species. The investigated residue positions are highlighted in blue, while the dots indicate omitted portions of the protein sequence.

residue that may disturb local packing and contribute to the structural and dynamical changes observed in the simulations. This conservation pattern supports the functional importance of all four investigated residues.

In silico prediction of mutation-induced protein stability changes

To assess the potential effects of the investigated substitutions on MAO-A protein stability, mutation-induced stability changes were first evaluated using several computational predictors. These tools employ different computational approaches, including machine learning, deep learning, consensus prediction, structural descriptors, evolutionary information, and protein-flexibility analysis. Because the predictors use different definitions and sign conventions for ΔΔG, the results were interpreted according to the direction and overall consensus of the predicted effect rather than by directly averaging the numerical values.

All seven predictors classified the investigated substitutions as destabilizing, although the predicted magnitude varied among the methods. The predicted ΔΔG values and methodological characteristics of the individual tools are summarized in Table 2. R45W was consistently associated with reduced MAO-A stability, with most methods indicating a mild-to-moderate destabilizing effect. C266F and E446K showed stronger destabilizing tendencies according to several predictors, whereas V244I was generally predicted to exert only a weak effect, consistent with the conservative nature of the valine-to-isoleucine substitution. Importantly, none of the variants was uniformly predicted to cause severe destabilization across all methods. Instead, the results suggest predominantly mild-to-moderate reductions in intrinsic stability, with the magnitude of the effect depending on both the mutation and the prediction method.

Despite differences in the absolute ΔΔG estimates, the overall agreement among the prediction methods suggests that all four substitutions may adversely affect MAO-A stability to some extent. However, these predictions do not imply complete loss of the native fold and should be regarded as supportive computational evidence rather than direct proof of impaired expression, folding efficiency, solubility, or thermodynamic stability under experimental conditions. A definitive evaluation of protein folding and structural stability would require complementary experimental characterization, which falls beyond the scope of the present computational study. To provide an additional structure-based assessment and determine whether the predicted destabilizing tendencies were reflected in the actual behavior of the enzyme, we performed molecular dynamics simulations of the apo wild-type and mutant MAO-A systems and evaluated whether they retained stable global structural behavior in the absence of serotonin. The resulting trajectories were analyzed using backbone RMSD, radius of gyration, residue-wise RMSF, and secondary-structure content to assess global fold retention, compactness, and conformational flexibility. The RMSD, radius of gyration (Rg), and secondary-structure results are summarized in Table 3, while the residue-wise RMSF profiles are presented in Fig. S1.

The mutant systems exhibited only modest increases in backbone deviation relative to the wild type, with E446K showing the largest average deviation. In contrast, the radius of gyration remained nearly unchanged across all systems, indicating preservation of global protein compactness. The secondary-structure composition was likewise highly conserved, with comparable α-helical and β-structural content in the wild-type and mutant enzymes. Residue-wise RMSF profiles were broadly similar throughout the structured protein core, while

Parameter	DynaMut2	DDMut	DUET	INPS-MD	PremPS	I-Mutant +	DeepDDG
R45W	−1.4	−1.7	−0.7	−1.2	+1.0	−0.9	−0.6
C266F	−1.1	−2.4	−1.3	−0.8	+0.4	−1.1	−2.5
E446K	−0.5	−1.5	−2.6	−1.2	+1.5	−0.6	−2.7
V244I	−0.4	−0.4	−0.3	−0.2	+0.5	−0.6	−0.4
Method type	Structure-based machine learning	Structure-based deep learning	Consensus structure-based predictor	Machine-learning predictor	Structure-based machine learning	Sequence- and structure-based machine learning	Structure-based deep neural network
Predicted stability metric	Mutation-induced change in protein thermodynamic stability	Mutation-induced change in protein stability free energy	Mutation-induced change in protein folding stability	Mutation-induced change in protein thermodynamic stability	Difference in protein unfolding free energy between mutant and wild type	Mutation-induced change in protein unfolding free energy	Mutation-induced change in protein stability free energy
Main methodological principle	Local 3D interactions and protein flexibility	Graph-based local structure with forward and reverse mutations	Consensus of mCSM and SDM predictions	Sequence- and structure-based molecular descriptors	Structural, evolutionary, and energetic features	Sequence profiles, structure, and physicochemical features	Neural-network analysis of local sequence and structure
Predicted effect	Destabilizing	Destabilizing	Destabilizing	Destabilizing	Destabilizing	Destabilizing	Destabilizing

Table 2. In silico prediction of mutation-induced changes in MAO-A protein stability. Predicted ΔΔG values for the R45W, C266F, E446K, and V244I variants obtained using complementary sequence- and structure-based stability predictors. The methodological characteristics, predicted stability metric, and overall predicted effect of each method are also summarized. ΔΔG values are expressed in kcal mol^{-1}. Negative ΔΔG indicates destabilization for all predictors except PremPS, where positive ΔΔG indicates destabilization.

System	RMSD ± SD	Rg ± SD	Secondary structure (%) ± SD				
			α-helix	3_{10}-helix	β-structure	Turn/Bend	Coil
WT	1.5 ± 0.2	22.8 ± 0.0	30.1 ± 0.3	4.3 ± 0.3	19.1 ± 0.3	27.5 ± 0.5	19.0 ± 0.4
E446K	1.9 ± 0.5	22.8 ± 0.1	29.9 ± 0.2	4.5 ± 0.2	19.5 ± 0.3	27.0 ± 0.1	19.2 ± 0.3
C266F	1.6 ± 0.1	22.8 ± 0.0	30.5 ± 0.6	4.6 ± 0.2	18.8 ± 0.4	26.9 ± 0.4	19.2 ± 0.7
V244I	1.8 ± 0.5	22.8 ± 0.0	30.3 ± 0.5	4.4 ± 0.4	19.1 ± 0.1	27.5 ± 0.1	18.7 ± 0.3
R45W	1.7 ± 0.1	22.8 ± 0.0	30.3 ± 0.4	4.5 ± 0.4	19.2 ± 0.0	27.2 ± 0.2	18.9 ± 0.2

Table 3. Global structural stability, compactness, and secondary-structure composition of apo wild-type and mutant MAO-A systems. Values are reported as mean ± SD from three independent simulations. RMSD quantifies the average deviation of the protein backbone from the reference structure, whereas Rg reflects overall protein compactness. Secondary-structure content describes the proportion of residues adopting defined local backbone conformations, thereby indicating whether the overall fold is preserved or whether ordered structural elements are lost during the simulations. β-structure combines β-sheet and β-bridge assignments, while Turn/Bend combines turn and bend assignments.

the largest differences were confined mainly to flexible terminal regions (Fig. S1). Collectively, these results indicate that the predicted destabilizing effects were not accompanied by global unfolding or substantial loss of compactness over the simulated timescale, but rather by modest and predominantly region-specific changes in conformational dynamics. This interpretation is consistent with the subsequent serotonin-bound simulations, in which the variants likewise retained the overall MAO-A fold while exhibiting mutation-dependent changes in local structure and dynamics.

Docking of Serotonin into the MAO–A Active Site

Serotonin (5–hydroxytryptamine) is a structurally complex monoamine neurotransmitter consisting of an indole ring system connected to a flexible ethylamine side chain. The primary amine group on this side chain is a central determinant of its chemical behavior, characterized by an experimental pK_a value of approximately 9.8. Consequently, at a physiological pH of 7.4, serotonin exists predominantly (>99%) in its protonated (cationic) form, referred to here as SRP (Fig. 2). Despite the prevalence of this charged species, the catalytic mechanism of MAO enzymes, which involves the oxidative deamination of the substrate to an imine intermediate (Scheme 1), is widely understood to require the neutral (unprotonated) form, SRN, for the rate–limiting chemical step[19,22,23]. This creates a mechanistic 'paradox' common to many amine–processing enzymes: while the enzyme must recruit the cationic substrate from the aqueous environment through favorable electrostatic interactions, the reaction itself proceeds from the neutral state[24,25]. Literature suggests that the enzyme's active site environment, often characterized by a hydrophobic 'aromatic cage' (including residues such as Tyr407 and Tyr444), helps stabilize the substrate while facilitating the necessary deprotonation prior to the hydride abstraction from the substrate's α–carbon atom onto the N5 atom of the FAD cofactor[23,26–28]. By docking both the protonated (SRP) and neutral (SRN) forms, this study aims to capture the dual nature of this process, examining how clinical

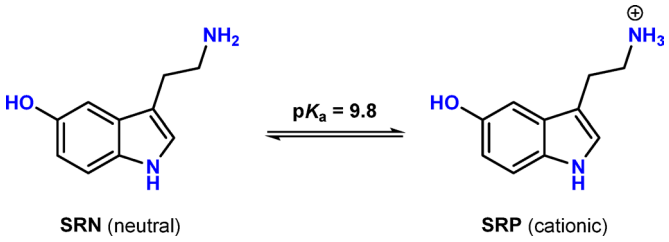
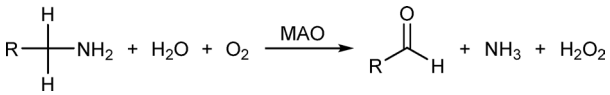


Fig. 2. Chemical structure of serotonin and its two protonation forms discussed in the text.



Scheme 1. The overall amine conversion catalyzed by MAO enzymes, during which the FAD cofactor is fully reduced into $FADH_2$. The reaction is established through the rate-limiting C(α)–H hydride abstraction followed by the amine N–H deprotonation. The resulting imine is then nonenzymatically hydrolyzed into the final aldehyde.

mutations impact both the initial recruitment of the physiological cation and the subsequent stability of the reactive neutral species.

The initial structures for the simulations were obtained by docking both the protonated (SRP) and neutral (SRN) forms of serotonin into the active site of the MAO–A enzyme. The most promising binding poses were selected based on their predicted binding affinity and structural suitability. Among these, the pose exhibiting reactive positioning within the active site, along with the formation of key hydrogen bonds and appropriate intermolecular distances, was chosen for further studies. Notably, both protonation states showed the same predicted binding affinities of − 6.6 kcal/mol. This protocol was employed to ensure a consistent starting point for direct comparison between the wild–type and mutant systems, such that any observed differences arise solely from the introduced mutations. The C266F mutation involves substitution of cysteine with phenylalanine, introducing a bulkier aromatic side chain. The R45W mutation replaces arginine with tryptophan, resulting in a larger and more hydrophobic residue. The V244I mutation corresponds to substitution of valine with isoleucine, differing by only one methyl group and representing a conservative change with a slight increase in side–chain volume. In the case of E446K, glutamate is replaced by lysine, introducing a change in both size and charge, from an anionic to a cationic residue. Overall, these substitutions comprise quite a diverse set of physicochemical perturbations, ranging from conservative changes in side-chain volume to pronounced alterations in charge, hydrophobicity, and aromatic character.

To further validate the selected binding mode, an additional docking protocol was performed in which each mutant structure was independently energy–minimized prior to docking. The resulting binding poses were then compared to the initially selected orientation. The ligand adopts a highly similar binding mode across all systems, maintaining a consistent orientation within the active site. The docking energies remain comparable, with values of − 6.5 kcal/mol for the wild–type and between − 6.3 and − 6.0 kcal/mol for the mutants. This is further supported by low protein RMSD values (~ 0.7–0.8 Å) and relatively small deviations in ligand positioning (SRP RMSD 0.6–2.3 Å), indicating that the ligand occupies a similar spatial position across all systems. Only minor local adjustments are observed, while the overall binding mode remains conserved. Detailed numerical data and representative structural overlays are provided in the Supplementary Information (Fig. S2).

In addition, the docking protocol was validated by re–docking the co–crystallized ligand harmine into the MAO–A active site. The resulting pose closely reproduced the experimental binding mode, with an RMSD of 0.9 Å and a predicted binding affinity of − 8.2 kcal/mol, confirming the reliability of the docking procedure (Fig. S3).

Overall, these observations indicate that the binding pose selected in the initial protocol is a plausible representation of the ligand orientation in the active site, as a similar binding mode is independently reproduced using the alternative docking procedure.

Molecular dynamics simulations of serotonin in the MAO–A active site

Molecular dynamics (MD) simulations were performed to investigate the behavior of serotonin within the active site of MAO–A in both the wild–type and mutant systems. Both the neutral (SRN) and protonated (SRP) forms of serotonin were considered. For each system, three independent replicas of 0.5 μs were carried out to ensure sufficient conformational sampling. All simulations were initiated from the same docking–derived binding pose. The analysis focused on the stability of ligand positioning, its orientation relative to the FAD cofactor, and the persistence of key interactions with active site residues over the course of the simulations. Importantly, additional MD simulations were performed to validate the initial protocol in which all systems were initiated from the same docking–derived binding pose. Specifically, three independent 200 ns replicas were carried out for each system generated via the alternative protocol, in which the mutant structures were first

energy–minimized and subsequently used for docking prior to the MD simulations. The results confirm that this approach is justified, as the ligand maintains a consistent and stable orientation regardless of the preparation protocol. This demonstrates that starting from the same binding pose is a reliable strategy for directly assessing the effect of mutations on ligand behavior within the active site.

In all analyzed trajectories, the neutral form of serotonin exhibits pronounced positional instability and does not maintain a stable binding conformation within the active site. The ligand fails to establish persistent interactions with neighboring amino acid residues or with the FAD cofactor and instead undergoes significant reorientation throughout the simulations. Three dominant non–productive binding poses are observed. In one of these, the ligand is displaced below or behind the FAD cofactor, effectively moving away from the reaction-relevant region of the active site (Fig. S4A). In another, the substrate is flipped such that the reactive carbon atom is directed away from the FAD, preventing a geometry suitable for reaction (Fig. S4B). In the third pose, the ligand adopts a nearly horizontal orientation relative to the FAD where a tyrosine residue partially blocks the access pathway (Fig. S4C), or is shifted toward the side of the active site, slipping beneath one of the tyrosine residues and escaping the sandwich–like arrangement that normally stabilizes serotonin (Fig. S4D). All three configurations are incompatible with a productive binding geometry. A properly oriented, reaction-competent pose is observed only transiently, typically at the beginning of the simulations. This orientation is rapidly lost as the trajectories progress, indicating that it does not correspond to a stable binding state under dynamic conditions. The loss of this pose is accompanied by increased ligand mobility and reorganization within the binding pocket. In some trajectories, the tyrosine residue that normally stabilizes the substrate adopts conformations that partially obstruct the access channel, further contributing to ligand displacement and preventing re–establishment of a productive orientation. Overall, the behavior of the neutral form suggests that it is unable to maintain a stable binding orientation compatible with the enzymatic reaction within the MAO-A active site. Despite occupying the binding pocket, the ligand predominantly samples non–productive configurations and lacks sustained interactions with the FAD and key surrounding residues.

In contrast, the protonated form (SRP) consistently maintains a stable binding orientation across all systems. Therefore, subsequent analyses were focused exclusively on the protonated form, as it represents the binding state of serotonin in the MAO-A active site that is both structurally stable and properly oriented for the enzymatic reaction.

Structural stability and distance–based analysis

Prior to the quantitative analysis, a structural inspection of the wild–type active site was performed in order to determine the spatial position of the mutation sites and their potential involvement in interactions with the FAD cofactor and the bound ligand. Residue C266 is located ~ 14 Å from the adenine moiety of the FAD cofactor and does not form any direct interactions with either the cofactor or the substrate. In contrast, residue E446 is positioned closer to the isoalloxazine ring of FAD (~ 5 Å) and forms a hydrogen bond with Tyr433, highlighting its role in stabilizing the local interaction network within the active site. Residue V244 is situated directly above the adenine moiety of the FAD cofactor (~ 4 Å) and is involved in the formation of two hydrogen–bonding interactions within this region. These interactions likely contribute to the stabilization of the FAD conformation by reinforcing the hydrogen–bonding network surrounding its ribityl chain. Similarly, residue R45 is located near the ribose ring of the FAD cofactor (~ 4 Å), where it forms a hydrogen bond with the ribose unit, likely contributing to the structural stabilization of the cofactor. Serotonin forms two key hydrogen bonds: one with the left side of the isoalloxazine ring of the FAD cofactor and another with Tyr444, supporting a stable binding orientation properly positioned for the enzymatic reaction within the active site. These structural observations (Fig. 3) provide a basis for interpreting the differences observed in the subsequent molecular dynamics simulations analyses.

As a first step in the analysis of the MD trajectories, root–mean–square deviation (RMSD) was evaluated to assess the overall structural stability of the systems. All systems exhibit similar RMSD profiles (Fig. S5), characterized by an initial increase followed by convergence to stable values, indicating equilibration of the structures. The wild–type system displays slightly lower RMSD values compared to the mutants, while the mutant systems show modestly higher deviations. However, these differences are relatively small and remain within a narrow range, with average RMSD values of approximately 1.3 Å for the wild–type and 1.5–1.9 Å for the mutants. Overall, the RMSD analysis indicates that all systems remain structurally stable throughout the simulations, with no evidence of significant conformational changes or major structural rearrangements induced by the mutations. A similar trend is observed for the ligand RMSD (Fig. S6). Serotonin remains relatively stable within the binding pocket across all systems, with only moderate fluctuations over time. The wild–type system exhibits the lowest ligand RMSD values (~ 0.30 Å), while the mutants show slightly higher deviations, typically in the range of ~ 0.35–0.45 Å. Despite these differences, the variations are modest and do not indicate significant displacement of the ligand from the active site.

To further characterize ligand active site positioning, additional distance–based analyses were performed focusing on key geometric features relevant for reaction. In particular, the distance between the reactive α–carbon atom of serotonin and the N5 atom of the FAD cofactor (C···N), associated with the hydride transfer step, was monitored throughout the simulations. The fraction of simulation time during which this distance (≤ 5 Å) was used to estimate the population of bound states. In addition, hydrogen–bond interactions between serotonin and the isoalloxazine ring of the FAD cofactor were analyzed by monitoring N–H···O hydrogen bonds. Furthermore, to assess mutation–specific effects on the local interaction network, hydrogen bonds involving key residues in proximity to the FAD cofactor and serotonin were also monitored (Table 4). This included interactions between serotonin and Tyr444, as well as residue–specific contacts such as FAD–R45, FAD–V244, and E446–Tyr444, enabling direct evaluation of how individual mutations alter stabilizing interactions within the system. In contrast, residue C266 is located too far from both the FAD cofactor and the ligand to form direct

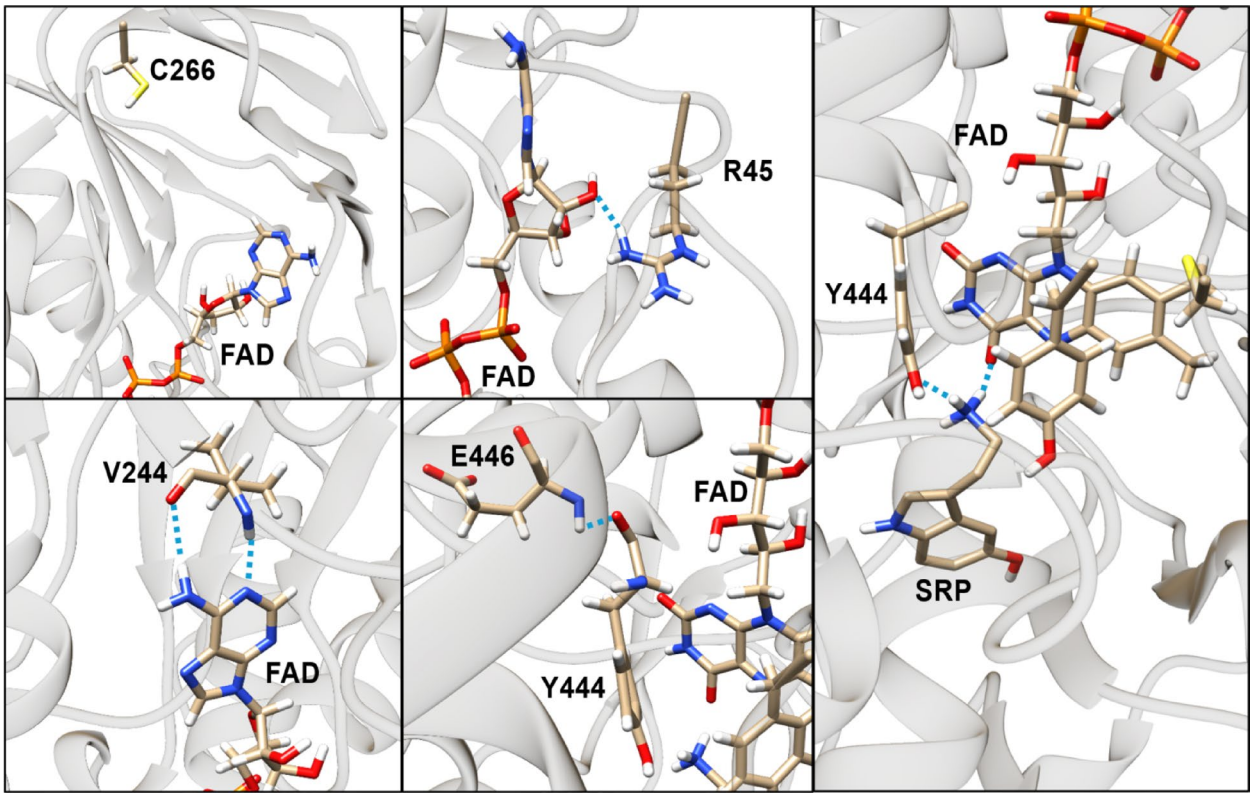


Fig. 3. Structural Overview of Mutation Sites in wild–type MAO–A enzyme. Illustration of the interaction of the mutation sites (C266, R45, V244, E446) with the FAD region, as well as illustration of the interactions between serotonin (SRP) and FAD, together with key stabilizing amino acid residues within the binding pocket. Hydrogen bonds between residues, FAD, and serotonin are indicated by cyan dashed lines, reflecting their role in stabilizing the system and supporting proper substrate orientation for reaction.

	WT	E446K	C266F	V244I	R45W
Bound (≤ 5 Å)					
FAD – SRP (C–N)	91.5	44.7	80.7	36.5	84.9
H–bond (≤ 3.5 Å)					
FAD – SRP (N–H····O)	93.7	46.7	82.0	25.0	85.1
SRP – Y444 (N–H····O)	64.0	35.6	46.7	29.2	48.9
FAD – R45 (N–H····O)	97.4				0.0
FAD – V244 (N–H····N)	98.4			92.8	
FAD – V244 (N–H····O)	81.4			67.8	
E446 – Y444 (N–H····O)	87.8	50.6			

Table 4. Hydrogen–bond occupancy (%) between serotonin, FAD, and key residues, reflecting mutation–induced disruption of stabilizing interactions in the MAO–A enzyme. The "Bound" state (≤ 5 Å) corresponds to the C–N5 distance between serotonin and the FAD cofactor, used as a criterion for reaction-relevant configurations. Only structurally relevant hydrogen–bond interactions are included for each system, with all values expressed as the percentage of simulation time (%) over three independent replicas. Column headings indicate the wild-type enzyme and the corresponding MAO-A mutant variants.

interactions, indicating that any effects of the C266F mutation are likely mediated through indirect or long–range structural perturbations.

As summarized in Table 4, the wild-type predominantly samples conformations with a geometry suitable for the enzymatic reaction, with the C···N distance remaining within 5 Å for over 90% of the simulation time (~ 91%). In contrast, all mutant systems show a reduced population of such configurations, with the most pronounced decrease observed in the V244I (~ 36%) and E446K (~ 45%) mutants. Consistent with this trend, hydrogen–bond occupancy analysis reveals that the wild–type system exhibits highly persistent N–H···O interactions between serotonin and the FAD cofactor (~ 98%) as well as with Tyr444 (~ 64%), indicating strong stabilization of the

ligand within the binding environment. Across the mutant systems, both interactions are reduced. The FAD–SRP hydrogen bond decreases to ~ 54% in E446K and ~ 38% in V244I, while even in systems with higher occupancies, a reduction relative to the wild–type is observed. A similar trend is seen for the SRP–Tyr444 interaction, which drops to ~ 36% in E446K and ~ 29% in V244I, and remains consistently reduced across all mutants. Notably, none of the mutants shows a more persistent interaction than the wild type for any of the tabulated descriptors, supporting a consistent mutation-induced reduction in the stability of the serotonin-bound state. However, because hydrogen-bond occupancy reflects the persistence of a contact rather than its intrinsic strength, these results should be interpreted as qualitative evidence for reduced stability of key interactions rather than as a quantitative measure of their energetic contribution.

Mutation–specific effects are further evident from interactions involving residues directly connected to the FAD cofactor. In the wild–type system, residue R45 forms a nearly permanent N–H···O hydrogen bond with FAD (~ 98%), which is completely lost in the R45W mutant, indicating a direct disruption of this stabilizing interaction. Similarly, residue V244 participates in strong hydrogen–bonding interactions with FAD in the wild–type system (~ 98% and ~ 91%), which are reduced in the V244I mutant (~ 93% and ~ 87%), indicating weakening of cofactor stabilization in this region. In addition, the interaction between E446 and Tyr444 is significantly reduced in the E446K mutant (~ 88% to ~ 51%), indicating disruption of the local hydrogen–bonding network. Given that Tyr444 is a key active–site residue involved in stabilizing serotonin in a sandwich–like arrangement, this change likely contributes to reduced ligand stabilization. Overall, these results demonstrate that mutations lead to a systematic reduction in both the population of binding conformations suitable for the enzymatic reaction and the hydrogen–bonding network that stabilizes serotonin and the FAD cofactor within the enzyme, with the most pronounced effects observed for the V244I and E446K mutants.

Mutation–induced changes in residue–level flexibility

Building on the observed weakening of hydrogen–bonding interactions that stabilize serotonin and the FAD cofactor, root mean square fluctuation (RMSF) differences between mutant and wild–type systems were analyzed to assess mutation–induced changes in protein dynamics at the residue level (Fig. S7). This approach enables identification of residue–specific changes in flexibility induced by each mutation, highlighting both local and long–range dynamical perturbations within the enzyme structure (Fig. 4).

In the E446K variant, the mutation site (position 446) is located in close proximity to the FAD cofactor, and changes in flexibility originate at the nearest neighboring residue, Asn75 (~ 4 Å from the mutation site). From this position, the perturbation propagates in a *domino–like manner* through adjacent residues such as Gln74 and Gln147, leading to a cascade of flexibility changes that extend around the binding pocket. Importantly, these residues are not necessarily directly connected through a continuous structural pathway but are instead located near one another around the active site. Notably, the residues most affected by these changes belong predominantly to the second coordination shell surrounding the binding cavity, which defines the structural framework of the active site and contributes to maintaining its shape and packing around the catalytic residues. Increased flexibility is observed in several residues lining the substrate–binding pocket, including Val101, Ser497, Lys168. In contrast, key active–site residues such as Gln215, which contributes to substrate positioning and stabilization (~ 3 Å from the substrate), and Asp328, situated in proximity to the active–site residue Ile325 (~ 5 Å), exhibit reduced fluctuations, reflecting increased rigidity of the catalytic core. This redistribution of dynamics suggests that enhanced mobility in surrounding regions may influence the overall organization and compactness of the active site. Given the close proximity of the mutation site to the FAD cofactor (~ 4 Å), even subtle perturbations appear sufficient to induce these changes in local structural arrangement.

A similar propagation pattern is observed for the C266F mutation. Although the mutation site is located further from the FAD (~ 13 Å), the effect is not confined to the local environment. Instead, changes in flexibility extend across structurally connected regions that link the mutation site to the substrate–binding pocket. The perturbation propagates from Cys266 through nearby residues such as Glu262 and His12, and further toward the central region of the protein. Notably, this effect extends across the FAD cofactor itself and the nearby residue Tyr407, both of which remain comparatively rigid. The key active–site residue Phe208 exhibits increased flexibility, together with Gln215, suggesting enhanced mobility in regions directly involved in substrate interaction. In contrast, the region surrounding Leu354, which lies in close proximity to the active site and includes active–site residues Ile335, Thr336, Leu337, and Met350, which are important for maintaining the geometry and packing of the substrate–binding pocket, is predominantly rigid. Despite the greater distance of the mutation site from the FAD and binding pocket, the C266F mutation induces a long–range redistribution of dynamics, characterized by increased flexibility in selected active–site residues and rigidification of adjacent regions within the catalytic environment. This suggests a subtle but functionally relevant reorganization of the active site that may influence substrate positioning and ultimately catalytic efficiency.

In the case of the V244I mutation, the mutation site is positioned directly above the FAD cofactor (~ 3 Å), where it forms two hydrogen bonds with the cofactor. No pronounced local increase in flexibility is observed in residues adjacent to the mutation site, instead the perturbation is immediately transmitted through the FAD, which exhibits increased fluctuations. This behavior is consistent with the loss of a hydrogen bond between the residue and the cofactor, suggesting its role in FAD stabilization. From there, the effect propagates toward residues surrounding the substrate–binding pocket, including Met300, Cys398, Val101, and Lys168, as well as more distal regions such as Asp480, where altered flexibility is observed. This pattern suggests that the FAD cofactor acts as a conduit for transmitting the perturbation from the mutation site to the broader active–site environment. These observations indicate that, even in the absence of strong local perturbations in residues adjacent to the mutation site, the V244I mutation induces a redistribution of dynamics via the FAD cofactor, leading to increased flexibility in regions associated with substrate binding. This highlights the sensitivity of the active–site network, where even a subtle chemical change near the cofactor, such as the addition of a single CH_2

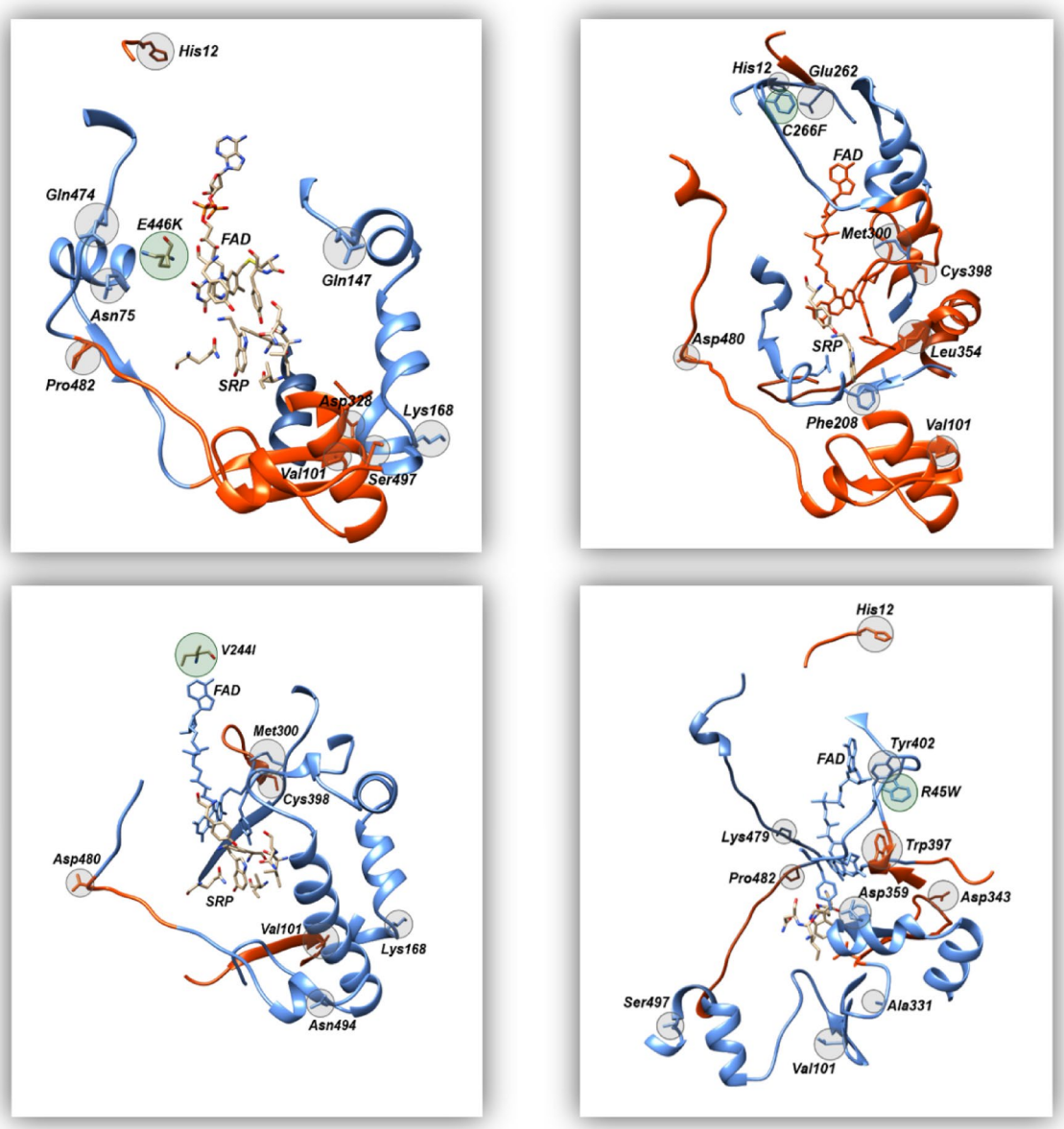


Fig. 4. Visual representation of mutation–induced changes in protein flexibility in the mutants. Structural mapping of selected residues exhibiting notable flexibility changes onto the protein structure, highlighting the spatial propagation of dynamical perturbations from the mutation site toward the binding pocket. The displayed flexibility changes represent RMSF differences between mutant and WT systems. Mutation sites are indicated by green circles, while residues exhibiting the largest fluctuation changes, identified based on RMSF differences, are marked with grey circles. The blue and red regions correspond to residues located within the shaded pink regions (see Fig. S6), which denote zones of highest fluctuation changes. Blue regions indicate increased flexibility, while red regions indicate decreased flexibility in the mutant relative to WT.

group in the V244I substitution, can propagate and influence the structural organization of the binding pocket, especially when the residue contributes to cofactor stabilization.

The R45W mutation exhibits a pronounced local effect, consistent with its close proximity to the FAD cofactor (~3.5 Å) and its involvement in hydrogen bonding with the cofactor. Significant changes in flexibility are observed in residues neighboring the mutation site, particularly Trp397 and Tyr402 (~3–4 Å), indicating a strong local perturbation of the surrounding structural environment. As observed for the V244I mutation, the perturbation is further transmitted through the FAD cofactor. However, in this case, it is associated with a complete loss of the hydrogen bond between the residue and FAD. This suggests a disruption of cofactor stabilization and is reflected in altered fluctuations of the FAD and its surrounding environment. The perturbation extends toward the central region of the protein, affecting residues such as Asp359 and Asp343, which are located near the binding pocket. Notably, flexibility changes are spatially asymmetric, predominantly affecting the side of the active–site cavity where the mutation is located. Residues such as Val101 and Ala331

show altered flexibility within this region, while more distal segments, including Ser497 and Lys479, also exhibit noticeable dynamical responses. The R45W mutation induces an uneven redistribution of dynamics, driven by the complete loss of a hydrogen bond and the accompanying change in residue charge from +1 (Arg) to 0 (Trp), leading to a redistribution of electrostatic interactions. This combination facilitates the propagation of the perturbation toward more distant residues, resulting in distinct regions of increased and decreased flexibility within the binding cavity. This asymmetric modulation suggests that different parts of the active site respond differently to the perturbation, potentially leading to imbalanced fluctuations within the pocket.

Overall, the RMSF analysis reveals a consistent trend across all mutants, where mutation–induced perturbations primarily affect residues in the second coordination shell surrounding the binding cavity, which defines the structural environment of the active site. These changes lead to increased flexibility in regions that support the pocket architecture, suggesting a more dynamically variable and less uniformly organized binding cavity. Notably, increased flexibility is consistently observed in loop regions around Val101 and Asp480, suggesting a potential role of these segments in regulating substrate access and mediating long–range dynamical communication within the enzyme.

Importantly, the observed flexibility changes are expected to have direct functional consequences for MAO-A activity. Rather than causing global structural destabilization, the mutations selectively perturb the dynamic network formed by second-shell residues that support the architecture of the substrate-binding pocket. Increased mobility of these regions is likely to facilitate transient opening ("breathing") of the active site, thereby increasing solvent accessibility and promoting water penetration into the catalytic cavity. Such changes are expected to weaken the hydrophobic environment required for efficient serotonin recognition and reduce the stability of key electrostatic and hydrogen-bonding interactions identified above. Consequently, the RMSF analysis provides a mechanistic link between the disease-associated mutations and the experimentally observed reduction in MAO-A function by demonstrating how subtle alterations in protein dynamics propagate to impair substrate binding.

To verify whether these mutation-induced flexibility changes translate into functional alterations of the binding pocket, additional analyses were performed to assess their effects on the physical properties of the active site (Table 5). In particular, the solvent–accessible surface area (SASA) of the binding pocket and the number of water molecules in its vicinity were evaluated.

As summarized in Table 5, all mutant systems exhibit an increase in both SASA and water occupancy relative to the wild–type, indicating enhanced solvent exposure of the binding pocket. The most pronounced effect is observed for the V244I mutant, which shows the largest increase in SASA (+61.2 $Å^2$) and water content (+4.6), suggesting substantial opening of the cavity. A similar but less pronounced trend is observed for the R45W and E446K mutants, which display moderate increases in SASA (+39.3 $Å^2$ and +29.8 $Å^2$, respectively) and water occupancy. The C266F mutant exhibits the smallest increase among the mutants (+16.6 $Å^2$ and +1.4), consistent with its more limited structural impact. These results indicate that mutation–induced changes in protein dynamics lead to increased solvent accessibility of the binding pocket, which may influence the stability of ligand binding and the overall organization of the active site.

Importantly, the increased amount of water molecules present at the active site in mutants may also contribute to the increased free energy barrier of the rate limiting step of serotonin degradation observed in our previous EVB calculations[20,21]. Specifically, an increased number of water molecules in the active site is expected to raise the effective local dielectric constant at the active site, thereby attenuating electrostatic interactions between the reaction center and its enzymatic surroundings. Since our previous results demonstrated that electrostatics plays a strongly catalytic role[21,29], with substantially greater stabilization in the transition state than in the reactant state, attenuation of these interactions may directly contribute to an increased reaction barrier and slower kinetics, in line with the observed effects on metabolites and the general clinical phenotype of affected individuals. Although the increased barrier in MAO-A variants has already been elucidated using EVB and charge-embedding methodology, it has not previously been directly connected to active-site water occupancy in the context of serotonin degradation. However, in our related histamine degradation study[30], water occupancy in/near the active site was used as a structural descriptor of catalytic performance, showing that reduced hydration of the hydrophobic MAO active site decreases dielectric shielding and enhances the catalytic electrostatic environment. The present results lead to an essentially analogous conclusion from the binding perspective, indicating that increased hydration of the predominantly hydrophobic active site is unfavorable not only for stable substrate binding but also for the chemical step.

System	*Mean SASA ($Å^2$)*	*Mean water mol. count*	*ΔSASA ($Å^2$)*	*ΔWater*
WT	43.1	3.0		
E446K	72.9	5.3	+29.8	+2.3
C266F	59.7	4.4	+16.6	+1.4
V244I	104.3	7.6	+61.2	+4.6
R45W	82.4	4.5	+39.3	+1.5

Table 5. Mutation–induced reduction of stabilizing interactions and increased flexibility lead to enhanced solvent exposure and water penetration in the MAO–A binding pocket.

Impact of mutation–induced dynamics on ligand binding affinity

To evaluate how the increased solvent exposure and water occupancy influence ligand binding affinity, MM/PBSA calculations were performed and decomposed into individual energetic contributions. As summarized in Table 6, all mutant systems exhibit less favorable binding free energies ($\Delta\Delta G$) compared to the wild–type, consistent with the previously observed disruption of stabilizing interactions and increased solvent accessibility within the binding pocket.

In contrast, van der Waals interactions (ΔE_{VDW}) show relatively minor and system–dependent variations. While R45W exhibits a slight unfavorable contribution (+1.1 kcal/mol), the remaining mutants display small stabilizing or near–neutral effects, suggesting that van der Waals interactions do not play a significant role in the observed differences in binding affinity. Although an increase in solvent exposure and water occupancy is observed, the corresponding nonpolar solvation contribution (ΔE_{SURF}), which is directly related to solvent–accessible surface area (SASA), remains relatively small ($\leq +0.16$ kcal/mol), indicating that changes in hydrophobic interactions are not the primary driver of the observed differences in binding affinity. Instead, the dominant effect arises from electrostatic contributions. Consistent with these findings, the total binding free energy (ΔG) becomes less favorable in all mutant systems. The largest loss of binding affinity is observed for V244I (+7.9 kcal/mol) and E446K (+7.5 kcal/mol), followed by R45W (+4.8 kcal/mol) and C266F (+2.9 kcal/mol). These results indicate that mutation–induced weakening of stabilizing interactions, together with increased solvent exposure, predominantly affects electrostatic interactions within the binding pocket, ultimately leading to reduced ligand binding affinity.

To further identify the origin of the unfavorable electrostatic contributions, a residue–level energy decomposition analysis was performed (Table S2). This approach enables identification of specific residues whose interactions with the ligand become less favorable upon mutation. The spatial arrangement of these key residues within the binding pocket is illustrated in Fig. 5. As shown in Table S2, several key residues within the binding pocket exhibit increased energetic penalties in the mutant systems, indicating weakened interactions with the ligand. Notably, the residues showing the largest unfavorable contributions are largely shared among the mutants, indicating that mutations, despite being quite different both in location as well as from physical perspective, perturb a common interaction network within the binding pocket rather than producing entirely mutation-specific energetic responses. This suggests that the reduced binding affinity arises from disruption of a shared set of ligand- and FAD-associated residues, including Gln215, Phe208, Leu337, Tyr444, and the FAD cofactor, with mutation-specific differences mainly reflected in the magnitude of these contributions.

In particular, the E446K mutant shows a substantial increase in unfavorable contributions from Gln215 (+1.5 kcal/mol), FAD (+1.8 kcal/mol), and Tyr444 (+0.8 kcal/mol), indicating a broad disruption of stabilizing interactions within the binding pocket. Notably, the mutation site itself also contributes unfavorably (+0.2 kcal/mol), further supporting its role in perturbing the local interaction network. Two key hydrogen bonds are significantly weakened in this system, the FAD–SRP interaction decreases from 97.6% in the wild–type to 54.4%, while the E446–Tyr444 interaction drops from 87.8 to 50.6%. To further characterize these changes, an additional analysis of N–H···O hydrogen bond between serotonin (SRP) and Gln215 was performed (Table S3). This analysis revealed that the SRP–Gln215 interaction also exhibits a pronounced decrease in occupancy, from 95.03% in the wild–type to 68.07% in the E446K mutant, consistent with the large unfavorable contribution observed for Gln215. The loss of the E446–Tyr444 hydrogen bond directly perturbs the positioning and interaction capability of Tyr444, which plays a central role in stabilizing serotonin through sidechain interactions. This disruption propagates toward neighboring residues, leading to weakening of the SRP–Gln215 interaction and reduced ligand stabilization. In parallel, destabilization of the local interaction network is reflected in increased energetic penalties associated with the FAD cofactor. These results indicate that the E446K mutation disrupts a key hydrogen–bonding pathway involving E446, Tyr444, serotonin, and Gln215, leading to a cascade of structural and energetic perturbations within the binding pocket.

A similar trend is observed for the V244I mutant, where increased unfavorable contributions are observed for Leu337 (+2.7 kcal/mol), Phe208 (+0.6 kcal/mol), Gln215 (+0.6 kcal/mol), FAD (+0.2 kcal/mol) and Tyr444 (+1.6 kcal/mol), indicating a pronounced destabilization of the interaction network within the binding pocket. Notably, residue V244 is positioned directly above the adenine moiety of the FAD cofactor, where it likely contributes to structural stabilization through hydrogen–bonding interactions. In the V244I mutant, these interactions are partially disrupted, as reflected by the reduced hydrogen–bond occupancy observed in the previous analysis, with the FAD–V244 N–H···N interaction decreasing from 100 to 92.8% and the N–H···O interaction from 90.9 to 86.9%. The slight loss of these stabilizing contacts weakens the local structural

System	*Mean ΔG*	*ΔΔG*	ΔE_{VDW}	$\Delta(E_{EL}+E_{GB})$	ΔE_{SURF}
WT	−26.55				
R45W	−21.89	+4.67	−0.74	+5.34	+0.06
C266F	−23.74	+2.81	−1.08	+3.85	+0.04
E446K	−19.18	+7.37	+1.10	+6.11	+0.16
V244I	−18.73	+7.83	−0.19	+7.86	+0.16

Table 6. Computed MM–PBSA binding affinities (ΔG) for serotonin substrate for several mutant MAO–A enzymes and their differences relative to the wild–type enzyme, together with specific contributions to the overall affinity. Detailed per–replica energy components used to compute these values are provided in Table S1. All values are in kcal mol^{-1}.

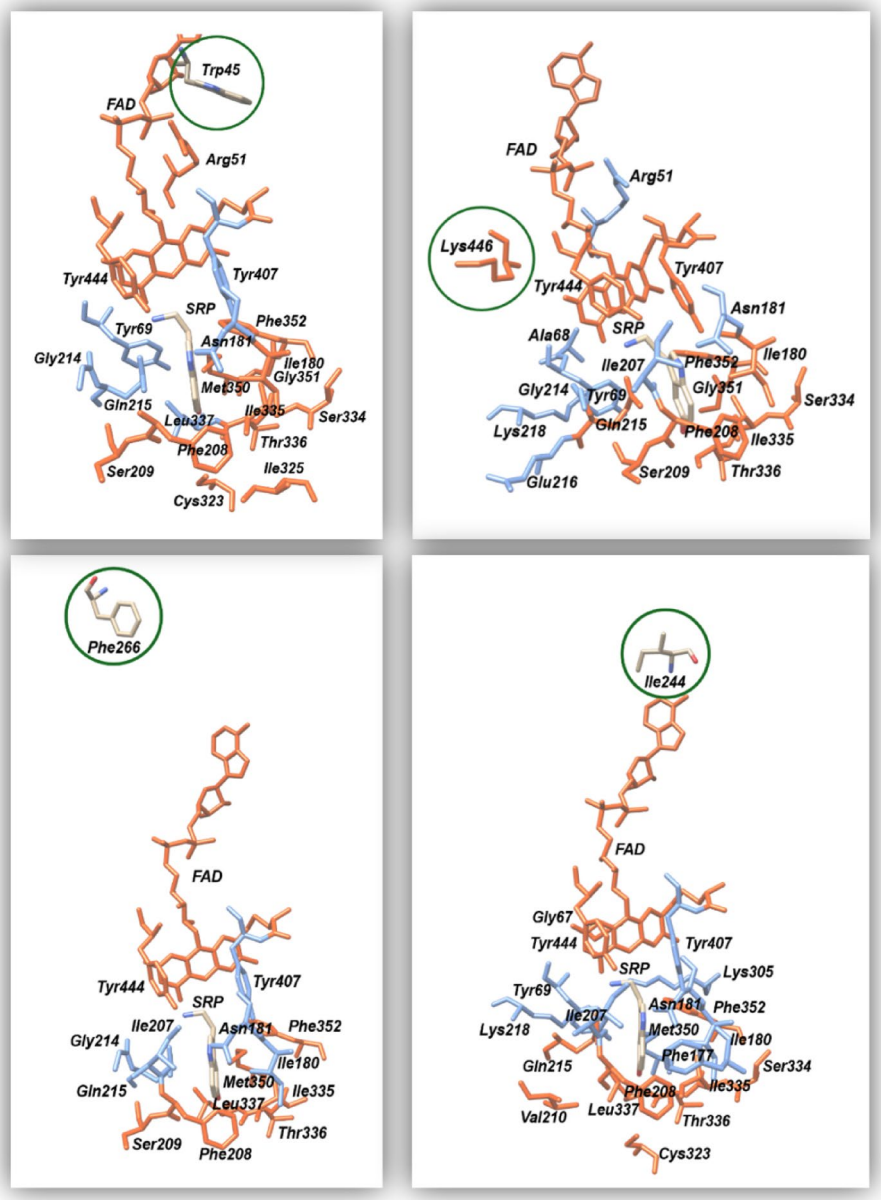


Fig. 5. Residue Contributions to Serotonin Binding in MAO–A Mutants. Structural representation of active–site residues, with unfavorable contributions to serotonin (SRP) binding shown in orange and stabilizing contributions in blue; mutation sites are indicated in green circle.

integrity of the FAD cofactor, which is further supported by the increased unfavorable backbone contribution associated with FAD. This disruption propagates to neighboring residues, including Tyr444, which shows increased energetic penalties and notably reduced hydrogen–bond occupancy with serotonin (from 64.0 to 29.2%), reflecting weakened stabilizing interactions. Furthermore, analysis of additional hydrogen bonds (Table S3) reveals that the SRP–Gln215 (N–H···O) interaction also decreases from 95.03 to 76.30%, supporting the observed unfavorable contribution associated with Gln215. A similar weakening trend is observed for the SRP–Phe208 interaction, which drops from 99.47 to 50.56%, as well as for the SRP–Leu337 hydrogen bond, decreasing from 47.79 to 27.88%. Together, these results indicate that the V244I mutation compromises the structural stabilization of FAD, triggering a cascade of structural perturbations that propagate to key active-site residues, including Leu337, Phe208, Gln215, and Tyr444, ultimately leading to reduced ligand stabilization.

The R45W mutant exhibits intermediate changes in residue–level contributions, with significant increases in unfavorable interactions, particularly for residues located on the right–hand side of the binding pocket, such as Phe208 (+0.8 kcal/mol), Thr336 (+0.7 kcal/mol), and Tyr444 (+1.0 kcal/mol). This spatial distribution is consistent with the position of residue R45, which is located on the right side of the ribose moiety of the FAD cofactor. As a result, the mutation induces perturbations that propagate toward this region of the binding

pocket, influencing residues beyond its immediate position within the interaction network. This is consistent with the complete loss of the FAD–R45 hydrogen bond observed in the mutant system, which decreases from 99.9% in the wild-type to 0.0% in R45W. In addition, several nearby hydrogen bonds are affected. The FAD–SRP (N–H···O) interaction shows a moderate decrease in occupancy, from 97.6 to 87.7%, while the SRP–Tyr444 (N–H···O) hydrogen bond is reduced from 64.0 to 48.9%, indicating weakened stabilization of serotonin through interactions with Tyr444. Analysis of additional hydrogen bonds (Table S3) reveals a pronounced decrease in the SRP–Phe208 (N–H···O) interaction from 99.47 to 45.52%, consistent with the increased unfavorable contribution of this residue. A similar weakening trend is observed for the SRP–Thr336 (O–H···N) interaction, which decreases from 91.74 to 59.39%, highlighting perturbations in this region of the binding pocket. Overall, the R45W mutation leads to disruption of the hydrogen-bonding network, predominantly affecting the right side of the binding pocket, primarily due to the loss of the FAD–R45 interaction and weakening of key contacts involving Phe208, Thr336, and Tyr444, which impair key interactions and consequently compromise ligand stabilization.

In contrast, the C266F mutant exhibits comparatively small changes in residue–level contributions, with all values remaining below ~ 1 kcal/mol, consistent with its lack of direct interactions with the FAD cofactor or active–site residues. However, despite being located distally from the active site, the mutation still induces subtle perturbations that propagate through the protein structure. Notably, the largest effects are observed for Phe208 (+ 0.4 kcal/mol), Thr336 (+ 0.4 kcal/mol), and Tyr444 (+ 0.9 kcal/mol), indicating that even distant mutations can influence key residues within the binding pocket. Analysis of hydrogen-bond occupancies (Table S3) reveals moderate decreases in several SRP–residue interactions. The SRP–Phe208 (N–H···O) hydrogen bond decreases from 99.47% in the wild-type to 74.75%, while the SRP–Thr336 (O–H···N) interaction is reduced from 91.74% to 70.82%. A similar trend is observed for the SRP–Leu337 interaction, which decreases from 47.79% to 33.77%, highlighting subtle perturbations in this region of the binding pocket. These effects extend through the previously mentioned second–shell residue fluctuations and reach the active–site region, where they influence the local interaction network. This observation highlights a distance–dependent effect of mutations, where residues closer to the active site exert a stronger impact on the interaction network, while more distant mutations, such as C266F, can still induce measurable but weaker long–range effects.

Taken together, the observed weakening of residue–level interactions is consistent with the increased solvent exposure of the binding pocket identified in the previous analysis. Notably, the active site of MAO–A is predominantly hydrophobic, and the increased presence of water molecules within the binding pocket is therefore energetically unfavorable. The penetration of solvent, facilitated by the previously observed fluctuations, into this hydrophobic environment alters the local dielectric properties and weakens electrostatic interactions between the ligand, FAD, and surrounding residues. This effect is reflected in the reduced favorable energetic contributions observed across key residues in the mutant systems. Overall, these results indicate that mutation–induced disruption of residue–level interactions, combined with increased solvent exposure of the hydrophobic binding pocket, leads to less favorable electrostatic interactions and reduced ligand stabilization.

Beyond elucidating the molecular basis of Brunner syndrome-associated mutations, the present findings also provide valuable insights for the rational design of future MAO-A ligands. The observed reduction in serotonin affinity arises primarily from mutation-induced changes in protein dynamics, active-site hydration, and electrostatic preorganization rather than from large structural rearrangements of the binding pocket. Consequently, future ligand optimization should extend beyond maximizing direct interactions with active-site residues and instead consider strategies that preserve favorable electrostatic complementarity and maintain stable binding despite increased active-site flexibility. Ligands capable of minimizing sensitivity to local dynamic fluctuations or compensating for mutation-induced electrostatic destabilization may exhibit improved binding robustness across different MAO-A variants. More broadly, these results highlight the importance of incorporating protein dynamics and hydration effects into structure-based drug design strategies targeting MAO-A and related enzymes.

Beyond explaining the molecular basis of Brunner syndrome-associated mutations, these findings may also inform the future design of MAO-A-targeting ligands. The present results suggest that successful ligand optimization should not only maximize direct interactions with catalytic residues but also preserve the electrostatic and hydration balance within the substrate-binding cavity. In particular, ligands capable of compensating for mutation-induced electrostatic destabilization or maintaining favorable interactions despite increased active-site flexibility may exhibit improved binding robustness across different MAO-A variants. More broadly, the identification of dynamic and energetic determinants governing substrate recognition provides a mechanistic framework that could support the rational development of next-generation MAO-A modulators with enhanced resilience to disease-associated structural perturbations.

Materials and methods

Multiple sequence alignment of MAO-A Orthologs

The evolutionary conservation of the investigated MAO-A residues was assessed by multiple sequence alignment of full-length MAO-A orthologs from 15 representative vertebrate species. Protein sequences were retrieved in FASTA format from UniProt[31] and aligned using Clustal Omega[32]. The selected species included human, non-human primates, domestic and laboratory mammals, birds, an amphibian, and fish. Residues corresponding to human MAO-A positions Arg45, Val244, Cys266, and Glu446 were identified from the resulting alignment and compared across the selected orthologs. In the Results section, only the sequence regions relevant to the investigated positions are shown, while the intervening portions of the aligned sequences are omitted.

In silico *protein stability prediction methods*

Mutation-induced changes in MAO-A protein stability were evaluated using seven complementary computational predictors, including DynaMut2[33], DDMut[34], DUET[35], INPS-MD[36], PremPS[37], I-Mutant+[38], and DeepDDG[39]. The wild-type MAO-A structure was used as the structural input for structure-based predictors, while the corresponding wild-type protein sequence was used where sequence information was required. Predictions were performed for the R45W, V244I, C266F, and E446K substitutions using the default settings of each server.

Preparation of MAO–A system

The starting structure for all calculations was a high–resolution (2.20 Å) X–ray crystal structure of monoamine oxidase A (MAO–A) in complex with harmine (PDB ID: 2Z5X)[10]. Crystallographic water molecules were removed prior to docking in order to allow bulk solvent molecules to access the active site during subsequent molecular dynamics equilibration and production simulations. The enzyme contains a covalently bound flavin adenine dinucleotide (FAD) cofactor linked to the conserved cysteine residue (Cys406)[12], which was parametrized in line with our earlier reports[20,21,27,40]. Protonation states of ionizable residues were assigned based on PROPKA3.1[41,42] predictions and further refined by inspection of the local hydrogen–bonding network. Missing hydrogen atoms were added using the tleap module in AmberTools21[43]. The mutant structures (V244I, E446K, R45W, and C266F) were generated using UCSF Chimera 1.18[44]. For each mutation, side–chain conformations were selected based on rotamers that minimized steric clashes and ensured favorable local interactions within the protein environment.

Molecular docking calculations

Following system preparation, docking simulations were performed using AutoDock Vina 1.2.7 algorithm[45,46], while the ligand and receptor files were prepared using AutoDockTools 1.5.7[47]. The scoring function accounts for dispersion interactions, hydrogen bonding, electrostatics, and desolvation effects to estimate the most probable binding conformations. Both neutral and protonated forms of serotonin were docked into the active site, while harmine was re–docked to validate the docking protocol[7,48,49]. The docking grid was centered on the active site with dimensions of $30 \times 30 \times 30$ points. During docking simulations, both the protein and ligands were treated as rigid.

Docking calculations were carried out using two approaches: (i) independent docking into the wild–type (WT) enzyme and selected mutants after minimization of the structure, and (ii) docking into the WT structure followed by the introduction of mutations into the resulting complexes. The ten lowest–energy binding poses were analyzed, and representative favorable conformations were selected for subsequent molecular dynamics simulations.

Molecular dynamics simulations

Molecular dynamics (MD) simulations were performed at the National VEGA high–performance computing (HPC) cluster in Maribor, Slovenia. Geometry optimization and RESP charge calculations for the FAD cofactor, as well as for the neutral and protonated forms of serotonin, were carried out using Gaussian 16[50] at the B3LYP/6–31G(d) and HF/6–31G(d) levels. The protein was modeled using the AMBER ff14SB force field[51] and gaff2 for the ligand[52]. Docking–derived ligand (protonated and neutral serotonin) conformations were used as initial structures for complex preparation, after which the systems were solvated in a truncated octahedral box of TIP3P water molecules[53] with a 10.0 Å solvent buffer. The system was neutralized by the addition of Na^+ or Cl^- ions, depending on the net charge of the model (WT or mutants), which were distributed throughout the system to achieve overall charge neutrality under periodic boundary conditions. The systems were first subjected to energy minimization consisting of 10,000 steps of steepest descent followed by 20,000 steps of conjugate gradient optimization. This was followed by NVT equilibration carried out in four consecutive runs, each consisting of 10,000 steps, during which the system was gradually heated from 0 to 300 K using a Langevin thermostat. This was followed by NPT equilibration carried out in two consecutive runs, each consisting of 100,000 steps at a time step of 2 fs. Positional restraints were applied in the initial stages and were subsequently removed in the final stage, while the pressure was maintained at 1 atm using the Berendsen barostat. Particle Mesh Ewald[54] was used to treat long–range electrostatic interactions, while periodic boundary conditions were applied. All bonds involving hydrogen atoms were constrained using the SHAKE algorithm[55], enabling a 2–fs integration time step. Production molecular dynamics simulations were performed as three independent 500 ns replicas for each system (1.5 μs cumulative simulation time per system) using the CUDA version of AMBER 22.3[56]. In addition, three independent validation simulations, each lasting 200 ns, were performed to further assess the reproducibility of the observed structural and energetic trends. Overall, each protein system was simulated for a cumulative 2.1 μs. To independently evaluate structural stability in the absence of substrate, three additional 500 ns apo simulations were performed for the wild-type and each mutant system, corresponding to a cumulative simulation time of 1.5 μs per apo system. Visualizations of the results were created using Visual Molecular Dynamics (VMD) 1.9.4 software[57], PyMOL 3.1[58] and UCSF Chimera 1.18[44].

Structural analysis and calculations of MD trajectories

Structural analyses were performed on the MD trajectories to characterize the stability and key interactions within the system. Backbone RMSD and RMSF analyses were carried out over the entire trajectory using the Cpptraj module[59], part of AMBER 22.3[56], with respect to the initial structures of the MAO–A enzyme and serotonin, respectively. The C–terminal transmembrane helix was excluded from these analyses, as it is membrane–anchored in vivo and becomes artificially flexible in the absence of a lipid environment.

The radius of gyration was calculated using CPPTRAJ to assess changes in global protein compactness during the simulations[59]. Secondary-structure assignments were determined using the secstruct implementation of the

DSSP algorithm in CPPTRAJ[59,60]. Secondary-structure populations were grouped into α-helix, 3_{10}-helix, β-structure, Turn/Bend, and unassigned coil categories. β-structure comprised the combined β-sheet and β-bridge assignments, whereas Turn/Bend comprised the combined turn and bend assignments.

Hydrogen bond analysis and distance measurements were performed over the entire trajectory, focusing on key contacts within the system. In addition, the number of water molecules and the solvent–accessible surface area (SASA)[61,62] were evaluated for the binding pocket, defined by the active–site residues, FAD, and serotonin.

Binding free energy calculations

Binding free energy calculations, ΔG_{BIND}, of the MAO–A enzyme–serotonin complex were performed using the Molecular Mechanics/Generalized Born Surface Area (MM/GBSA) method[63–65] included in Amber 22 software. Calculations were performed on 25.000 snapshots from frame 200 onwards of the MD simulation, where the simulated system was considered fully equilibrated. We used the Generalized Born IGB method 5[66,67], and a 0.10 M salt concentration. Within this approach, ΔG_{BIND} is calculated as[68,69]:

$$\Delta G_{\mathrm{BIND}} = < G_{\mathrm{complex}} > - < G_{\mathrm{enzyme}} > - < G_{\mathrm{inhibitor}} > \quad (1)$$

where the symbol < > represents the average value over all snapshots. The free energy of a system can be approximated by three terms:

$$G_{\mathrm{complex/enzyme/inhibitor}} = E_{\mathrm{MM}} + G_{\mathrm{solv}} - \mathrm{T} \times \Delta S_{\mathrm{MM}} \quad (2)$$

where E_{MM}, the gas-phase molecular mechanical energy, is obtained as a sum of $E_{internal}$, E_{VDW}, and E_{elec} contributions. G_{solv}, the solvation free energy, is a sum of polar (G_{polar}) and nonpolar ($G_{nonpolar}$) components, with the former calculated by solving the finite-difference Generalized Born equation, while the latter was determined on the basis of the solvent-accessible surface area (SASA) as:

$$G_{\mathrm{nonpolar}} = \gamma \times \mathrm{SASA} + \beta \quad (3)$$

with recommended empirical parameters γ = 0.0054 kcal mol^{-1} $Å^{-2}$ and β = 0.92 kcal mol^{-1}[64]. The solute conformational entropy (S_{MM}) was estimated by the normal-mode analysis. The interior and exterior dielectric constants were set to 1 and 80, respectively[70]. The MM–GBSA binding free energies were decomposed on a per–residue basis using an established protocol, allowing identification of individual residue contributions to ΔG_{BIND} in terms of interaction, solvation, and entropic components.

Conclusions

In this study, we have provided a detailed molecular–level investigation into how disease-associated mutations in MAO–A, namely C266F, V244I, E446K, and R45W, disrupt enzyme–substrate interactions. Our findings reveal that all investigated variants exhibit significantly reduced binding affinity for serotonin. This loss of affinity is primarily driven by unfavorable electrostatic contributions and a weakening of key stabilizing hydrogen bonds, such as those with Tyr444 and the FAD cofactor.

These results complement and provide a structural rationale for previous studies that have focused on the catalytic consequences of these Brunner syndrome-related mutations. While earlier work using empirical valence bond simulations demonstrated that these specific variants lead to significantly reduced catalytic efficiency and slower reaction rates for serotonin degradation[19–21], our current research identifies the binding–stage perturbations that precede the chemical step. Importantly, our findings indicate that the observed loss of affinity does not arise from major structural rearrangements but rather from subtle mutation–induced perturbations in protein dynamics and geometry. Furthermore, these findings highlight a critical limitation for the rational design of artificial mutant enzymes based on electrostatic premises. As we recently demonstrated using EVB simulations and charge-embedding electrostatics, point mutations in MAO–A do not merely act as localized electrostatic perturbations. Rather, they induce highly dislocated, subtle structural shifts, often less than 0.5 Å, that are smeared over the entire enzyme scaffold[21]. Strikingly, even minimal displacements of ~ 0.2 Å in key domains near the active site are sufficient to substantially alter a residue's electrostatic contribution to catalysis, causing distal mutations (like C266F) to yield significant performance reduction comparable to those of local charge-altering mutations (like E446K). The present study reaches an almost identical conclusion using different molecular dynamics methodologies focused on substrate binding, thereby validating our previous observations and treatments. Rather than a localized disruption, we observe a long-range dynamical reorganization that increases the flexibility of second-shell residues and enhances solvent penetration. Crucially, this increased hydration exerts a dual disruptive effect: the influx of water directly destabilizes the intrinsically hydrophobic pocket during substrate binding, while simultaneously raising the local dielectric constant, which attenuates the electrostatic preorganization catalyzing the subsequent chemical transition state. Together, these synergistic findings underscore the immense complexity of protein structural dynamics and interaction networks. Because mutation-induced effects involve such extensive, long-range reorganization that critically affects both the preorganized electrostatics of the reaction center and the binding of the substrate, attempts to design improved enzymes based solely on the localized optimization of specific residues are exceedingly difficult. Successful rational design must inherently account for the highly coupled, global structural environment of the entire protein scaffold.

Furthermore, the vulnerability of MAO–A to reduced substrate binding extends beyond genetic factors to include external physiological stressors. Recent computational evidence has shown that the SARS–CoV–2 spike protein, particularly from the more contagious South African B.1.351 variant, can form stable complexes

with MAO–A with an affinity comparable to its recognition of the ACE2 receptor[71]. These spike–protein interactions significantly alter the enzyme's electrostatic environment, leading to a marked dysregulation of its affinity for physiological substrates like serotonin. Ultimately, our data suggests that the impaired enzymatic function characteristic of MAO–A deficiency, whether arising from genetic mutations or viral interference, is a cumulative effect of reduced initial recruitment of the substrate and decreased catalytic efficiency. This integrated view provides a more comprehensive understanding of the molecular mechanisms underlying neurotransmitter misbalances and their links to neurodegenerative and neuropsychiatric disorders.

Data availability

The wild-type MAO-A structure used in this work was obtained from the RCSB Protein Data Bank (https://www.rcsb.org/) under accession code 2Z5X. All files required to reproduce the reported results, together with representative structures generated during this study, have been deposited in a publicly available GitHub repository: https://github.com/martinarajic/maoa-brunner-serotonin-binding.

Received: 15 June 2026; Accepted: 31 July 2026
Published online: 05 August 2026

References

1. Ramsay, R. R. Monoamine oxidases: The biochemistry of the proteins as targets in medicinal chemistry and drug discovery. *Curr. Top. Med. Chem.* **12**(20), 2189–2209 (2012).
2. Youdim, M. B., Edmondson, D. & Tipton, K. F. The therapeutic potential of monoamine oxidase inhibitors. *Nat. Rev. Neurosci.* **7**(4), 295–309 (2006).
3. Grimsby, J. et al. Tissue distribution of human monoamine oxidase-A and oxidase-B messenger-RNA. *J. Neurochem.* **55**(4), 1166–1169 (1990).
4. Shih, J. C., Chen, K. & Ridd, M. J. Monoamine oxidase: From genes to behavior. *Annu. Rev. Neurosci.* **22**, 197–217 (1999).
5. Westlund, K. N. et al. Distinct monoamine oxidase-A and oxidase-B populations in primate brain. *Science* **230**(4722), 181–183 (1985).
6. Binda, C. et al. Structure of human monoamine oxidase B, a drug target for the treatment of neurological disorders. *Nat. Struct. Biol.* **9**(1), 22–26 (2002).
7. Binda, C. et al. Insights into the mode of inhibition of human mitochondrial monoamine oxidase B from high-resolution crystal structures. *Proc. Natl. Acad. Sci. U. S. A.* **100**(17), 9750–9755 (2003).
8. Fowler, C. J. & Tipton, K. F. On the substrate specificities of 2 forms of monoamine-oxidase. *J. Pharm. Pharmacol.* **36**(2), 111–115 (1984).
9. De Colibus, L. et al. Three-dimensional structure of human monoamine oxidase A (MAO A): Relation to the structures of rat MAO A and human MAO B. *Proc. Natl. Acad. Sci. U. S. A.* **102**(36), 12684–12689 (2005).
10. Son, S.Y., et al. Structure of human monoamine oxidase A at 2.2-Å resolution. The control of opening the entry for substrates/inhibitors. Proceedings of the National Academy of Sciences of the United States of America, 2008. **105**(15), 5739–5744
11. De Colibus, L. & Mattevi, A. New frontiers in structural flavoenzymology. *Curr. Opin. Struct. Biol.* **16**(6), 722–728 (2006).
12. Geha, R. M. et al. Analysis of conserved active site residues in monoamine oxidase A and B and their three-dimensional molecular modeling. *J. Biol. Chem.* **277**(19), 17209–17216 (2002).
13. Brunner, H. G. et al. Abnormal-behavior associated with a point mutation in the structural gene for monoamine oxidase-A. *Science* **262**(5133), 578–580 (1993).
14. Cases, O. et al. Aggressive-behavior and altered amounts of brain-serotonin and norepinephrine in mice lacking Maoa. *Science* **268**(5218), 1763–1766 (1995).
15. Piton, A. et al. A second mutation in MAOA identified by targeted high-throughput sequencing in a family with altered behavior and cognition. *Eur. J. Hum. Genet.* **22**(6), 776–783 (2014).
16. Palmer, E. E. et al. New insights into Brunner syndrome and potential for targeted therapy. *Clin. Genet.* **89**(1), 120–127 (2016).
17. Popp, B. et al. Exome pool-seq in neurodevelopmental disorders. *Eur. J. Hum. Genet.* **25**(12), 1364–1376 (2017).
18. Peters, T. M. A. et al. Monoamine oxidase A activity in fibroblasts as a functional confirmation of MAOA variants. *JIMD Rep.* **58**(1), 114–121 (2021).
19. Prah, A. et al. How monoamine oxidase A decomposes serotonin: An empirical valence bond simulation of the reactive step. *J. Phys. Chem. B* **124**(38), 8259–8265 (2020).
20. Prah, A. et al. Brunner syndrome caused by point mutation explained by multiscale simulation of enzyme reaction. *Sci. Reports* **12**(1), 21889 (2022).
21. Rajic, M. & Stare, J. Investigation of electrostatic effects on enyzme catalysis: Insights from computational simulations of monoamine oxidase A pathological variants leading to the Brunner syndrome. *J. Chem. Inf. Model.* **65**(7), 3439–3450 (2025).
22. Poberznik, M. et al. Empirical valence bond simulations of the hydride-transfer step in the monoamine oxidase A catalyzed metabolism of noradrenaline. *J. Phys. Chem. B* **120**(44), 11419–11427 (2016).
23. Gaweska, H. & Fitzpatrick, P. F. Structures and mechanism of the monoamine oxidase family. *Biomol. Concepts* **2**(5), 365–377 (2011).
24. Jones, T. Z. E. et al. Variations in activity and inhibition with pH: The protonated amine is the substrate for monoamine oxidase, but uncharged inhibitors bind better. *J. Neural Transm.* **114**(6), 707–712 (2007).
25. Repic, M. et al. Examining electrostatic preorganization in monoamine oxidases A and B by structural comparison and pKa calculations. *J. Phys. Chem. B* **118**(16), 4326–4332 (2014).
26. Vianello, R., Repic, M. & Mavri, J. How are biogenic amines metabolized by monoamine oxidases?. *Eur. J. Org. Chem.* **2012**(36), 7057–7065 (2012).
27. Tandarić, T. & Vianello, R. Computational insight into the mechanism of the irreversible inhibition of monoamine oxidase enzymes by the antiparkinsonian propargylamine inhibitors rasagiline and selegiline. *ACS Chem Neurosci* **10**(8), 3532–3542 (2019).
28. Rajic, M., Prah, A. & Stare, J. Deciphering the two-step hydride mechanism of monoamine oxidase flavoenzymes. *ACS Omega* **9**(42), 43046–43057 (2024).
29. Prah, A. et al. Electrostatics as the driving force behind the catalytic function of the monoamine oxidase A enzyme confirmed by quantum computations. *ACS Catal.* **9**(2), 1231–1240 (2019).
30. Marsavelski, A. et al. Why monoamine oxidase B preferably metabolizes n-methylhistamine over histamine: Evidence from the multiscale simulation of the rate-limiting step. *Int. J. Mol. Sci.* **23**(3), 1910 (2022).
31. UniProt: the universal protein knowledgebase in 2025. Nucleic acids research, 2025. **53**(D1), D609–D617
32. Sievers, F. et al. Fast, scalable generation of high-quality protein multiple sequence alignments using Clustal Omega. *Mol. Syst. Biol.* **7**, 539 (2011).

33. Rodrigues, C. H., Pires, D. E. & Ascher, D. B. DynaMut2: Assessing changes in stability and flexibility upon single and multiple point missense mutations. *Protein Sci.* **30**(1), 60–69 (2021).
34. Zhou, Y. et al. DDMut: Predicting effects of mutations on protein stability using deep learning. *Nucleic Acids Res.* **51**(W1), W122–W128 (2023).
35. Pires, D. E., Ascher, D. B. & Blundell, T. L. DUET: A server for predicting effects of mutations on protein stability using an integrated computational approach. *Nucl. Acids Res.* **42**(W1), W314–W319 (2014).
36. Savojardo, C. et al. INPS-MD: A web server to predict stability of protein variants from sequence and structure. *Bioinformatics* **32**(16), 2542–2544 (2016).
37. Chen, Y. et al. PremPS: Predicting the impact of missense mutations on protein stability. *PLoS Comput. Biol.* **16**(12), e1008543 (2020).
38. Capriotti, E., Fariselli, P. & Casadio, R. I-Mutant2.0: Predicting stability changes upon mutation from the protein sequence or structure. *Nucl. Acids Res.* **33**(22), W306–W310 (2005).
39. Cao, H. et al. DeepDDG: Predicting the stability change of protein point mutations using neural networks. *J. Chem. Inf. Model.* **59**(4), 1508–1514 (2019).
40. Vrban, L. & Vianello, R. Prominent neuroprotective potential of indole-2-N-methylpropargylamine: High affinity and irreversible inhibition efficiency towards monoamine oxidase B revealed by computational scaffold analysis. *Pharmaceuticals (Basel)* **17**(10), 1292 (2024).
41. Olsson, M. H. M. et al. PROPKA3: Consistent treatment of internal and surface residues in empirical pKa predictions. *J. Chem. Theory Comput.* **7**(2), 525–537 (2011).
42. Sondergaard, C. R. et al. Improved treatment of ligands and coupling effects in empirical calculation and rationalization of pKa values. *J. Chem. Theory Comput.* **7**(7), 2284–2295 (2011).
43. Case, D. A. et al. *Amber 2021* (University of California, 2021).
44. Pettersen, E. F. et al. UCSF chimera - A visualization system for exploratory research and analysis. *J. Comput. Chem.* **25**(13), 1605–1612 (2004).
45. Trott, O. & Olson, A. J. Software news and update AutoDock Vina: Improving the speed and accuracy of docking with a new scoring function, efficient optimization, and multithreading. *J. Comput. Chem.* **31**(2), 455–461 (2010).
46. Eberhardt, J. et al. AutoDock Vina 1.2.0: New docking methods, expanded force field, and python bindings. *J. Chem. Inform. Model* **61**(8), 3891–38983 (2021).
47. Morris, G. M. et al. AutoDock4 and AutoDockTools4: Automated docking with selective receptor flexibility. *J. Comput. Chem.* **30**(16), 2785–2791 (2009).
48. Liu, K. & Kokubo, H. Prediction of ligand binding mode among multiple cross-docking poses by molecular dynamics simulations. *J. Comput. Aided Mol. Des.* **34**(11), 1195–1205 (2020).
49. Mateev, E. et al. Validation through re-docking, cross-docking and ligand enrichment in various well-resoluted MAO-B receptors. *Int. J. Pharm. Sci. Res* **13**(3), 1000–1007 (2022).
50. Frisch, M.J., et al., Gaussian 16 Rev. C.01. 2016: Wallingford, CT.
51. Maier, J. A. et al. ff14SB: Improving the accuracy of protein side chain and backbone parameters from ff99SB. *J. Chem. Theory Comput.* **11**(8), 3696–3713 (2015).
52. Wang, J. M. et al. Development and testing of a general amber force field. *J. Comput. Chem.* **25**(9), 1157–1174 (2004).
53. Jorgensen, W. L. et al. Comparison of simple potential functions for simulating liquid water. *J. Chem. Phys.* **79**(2), 926–935 (1983).
54. Darden, T., York, D. & Pedersen, L. Particle Mesh Ewald - an N.Log(N) method for ewald sums in large systems. *J. Chem. Phys.* **98**(12), 10089–10092 (1993).
55. Ryckaert, J. P., Ciccotti, G. & Berendsen, H. J. C. Numerical-integration of Cartesian equations of motion of a system with constraints - molecular-dynamics of N-alkanes. *J. Comput. Phys.* **23**(3), 327–341 (1977).
56. Case, D.A., et al., Amber 2022. 2022, University of California, San Francisco.
57. Humphrey, W., Dalke, A. & Schulten, K. VMD: Visual molecular dynamics. *J. Mol. Graph. Model.* **14**(1), 33–38 (1996).
58. Schrödinger, L.L.C., The PyMOL Molecular Graphics System, Version 2.0. 2015, Schrödinger, LLC: New York, NY USA.
59. Roe, D. R. & Cheatham, T. E. PTRAJ and CPPTRAJ: Software for processing and analysis of molecular dynamics trajectory data. *J. Chem. Theory Comput.* **9**(7), 3084–3095 (2013).
60. Kabsch, W. & Sander, C. Dictionary of protein secondary structure: Pattern recognition of hydrogen-bonded and geometrical features. *Biopolymers* **22**(12), 2577–2637 (1983).
61. Lee, B. & Richards, F. M. The interpretation of protein structures: Estimation of static accessibility. *J. Mol. Biol.* **55**(3), 379–400 (1971).
62. Shrake, A. & Rupley, J. A. Environment and exposure to solvent of protein atoms - lysozyme and insulin. *J. Mol. Biol.* **79**(2), 351–371 (1973).
63. Wang, C. H. et al. Recent developments and applications of the MMPBSA method. *Front. Mol. Biosci.* **4**, 87 (2018).
64. Kollman, P. A. et al. Calculating structures and free energies of complex molecules: Combining molecular mechanics and continuum models. *Acc. Chem. Res.* **33**(12), 889–897 (2000).
65. Genheden, S. & Ryde, U. The MM/PBSA and MM/GBSA methods to estimate ligand-binding affinities. *Expert Opin. Drug Discov.* **10**(5), 449–461 (2015).
66. Still, W. C. et al. Semianalytical treatment of solvation for molecular mechanics and dynamics. *J. Am. Chem. Soc.* **112**(16), 6127–6129 (1990).
67. Mongan, J. et al. Generalized born model with a simple, robust molecular volume correction. *J. Chem. Theory Comput.* **3**(1), 156–169 (2007).
68. Bao, H. et al. Ligand-mediated conformation diversity of Hsp90 revealed by GaMD simulations and Markov model. *Mol. Divers.* **30**, 4401–4420 (2025).
69. Chen, J. et al. Decoding the identification mechanism of an SAM-III riboswitch on ligands through multiple independent Gaussian-accelerated molecular dynamics simulations. *J. Chem. Inf. Model.* **62**(23), 6118–6132 (2022).
70. Bashford, D. & Case, D. A. Generalized born models of macromolecular solvation effects. *Annu. Rev. Phys. Chem.* **51**(1), 129–152 (2000).
71. Hok, L. et al. COVID-19 infection and neurodegeneration: Computational evidence for interactions between the SARS-CoV-2 spike protein and monoamine oxidase enzymes. *Comput. Struct. Biotechnol. J.* **20**, 1254–1263 (2022).

Acknowledgements

The authors gratefully acknowledge the HPC RIVR consortium (https://www.hpc-rivr.si) and EuroHPC JU (https://eurohpc-ju.europa.eu/) for granting computing resources of the HPC system VEGA at the Institute of Information Science (https://www.izum.si/en/home/) (Project ID: S24O02-06).

Author contributions

J.S., M.S.D., M.R., and J.M. designed the work, J.S., M.S.D., J.M. and R.V. supervised the work, M.R. performed computational simulations, M.R., L.V.Đ. and R.V. analysed and interpreted the results, M.R. prepared all tables

and graphical materials and drafted the work, all authors have revisited the text. J.S., J.M. and R.V. acquired the financial support for the project leading to this publication. All authors approved the submission version.

Funding
This work was supported by the Slovenian Research and Innovation Agency (ARIS) and the Croatian Science Foundation (HRZZ) through the Weave multilateral initiative. The Slovenian contribution was funded via program funding (P1-0012) and research project grants (J1-50022, N1-0404), including support for the Young Researcher grant awarded to M. R. The Croatian contribution was supported by the HRZZ project grant number IP-2024-05-3953.

Declarations

Competing interests
The authors declare no competing interests.

Additional information
Supplementary Information The online version contains supplementary material available at https://doi.org/10.1038/s41598-026-65452-1.

Correspondence and requests for materials should be addressed to R.V.

Reprints and permissions information is available at www.nature.com/reprints.

Publisher's note Springer Nature remains neutral with regard to jurisdictional claims in published maps and institutional affiliations.

Open Access This article is licensed under a Creative Commons Attribution 4.0 International License, which permits use, sharing, adaptation, distribution and reproduction in any medium or format, as long as you give appropriate credit to the original author(s) and the source, provide a link to the Creative Commons licence, and indicate if changes were made. The images or other third party material in this article are included in the article's Creative Commons licence, unless indicated otherwise in a credit line to the material. If material is not included in the article's Creative Commons licence and your intended use is not permitted by statutory regulation or exceeds the permitted use, you will need to obtain permission directly from the copyright holder. To view a copy of this licence, visit http://creativecommons.org/licenses/by/4.0/.

© The Author(s) 2026